Volume 9 | Number 7 | 7 April 2022

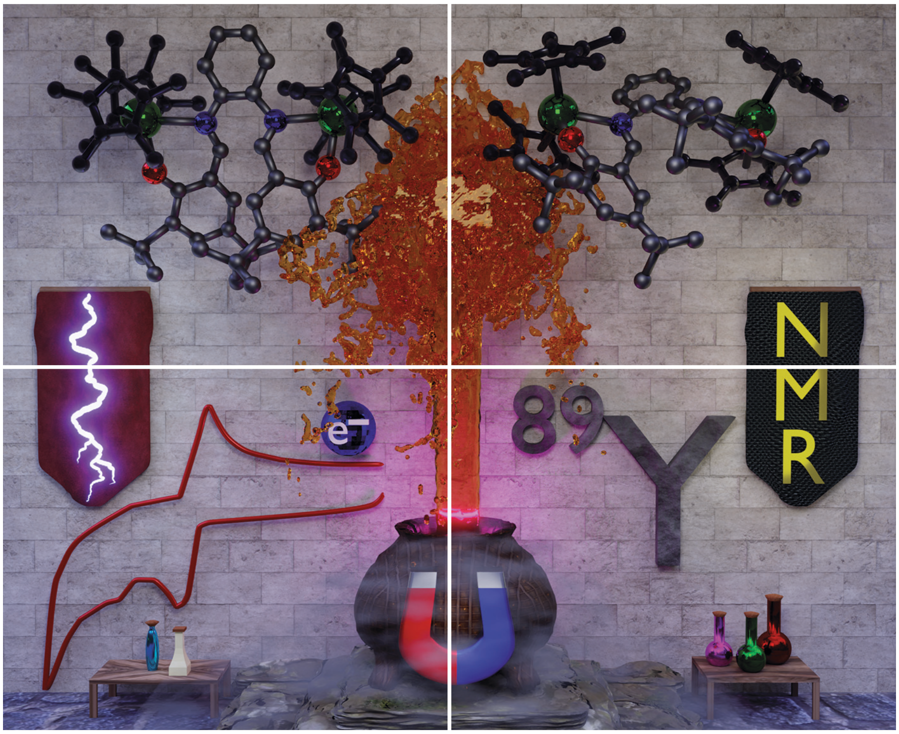

INORGANIC CHEMISTRY FRONTIERS

CCS 中国化学会 CHINESE CHEMICAL SOCIETY
PEKING UNIVERSITY 1898
ROYAL SOCIETY OF CHEMISTRY
rsc.li/frontiers-inorganic

INORGANIC CHEMISTRY
FRONTIERS

RESEARCH ARTICLE

Cite this: *Inorg. Chem. Front.*, 2022, **9**, 1325

Taming salophen in rare earth metallocene chemistry†

Ernesto Castellanos, Florian Benner and Selvan Demir *

A series of multinuclear metallocenes composed of a ^{tBu}salophen dianion bound to two rare earth metal ions, where each is encased in a bis-pentamethylcyclopentadienyl scaffold, was realized. The isolated molecules $(Cp^*_2RE)_2(\mu\text{-}^{tBu}salophen)$, where RE = Gd (**1**), Dy (**2**), and Y (**3**), constitute the first salophen-bridged metallocene complexes for any metal ion. **1–3** were characterised by X-ray crystallography, cyclic voltammetry, IR, NMR, and UV-Vis-NIR spectroscopy. Cyclic voltammograms of **1–3** excitingly exhibit quasi-reversable features attributed to the ($^{tBu}salophen^{2-}/^{tBu}salophen^{3-\bullet}$) redox couple. DFT calculations on **3** uncovered the highest occupied molecular orbital to be primarily localized on the metallocene and phenolate moieties of the ^{tBu}salophen ligand. Furthermore, the nuclear spin $I = \frac{1}{2}$ for yttrium allowed the collection of ^{89}Y NMR spectra for **3**. Magnetic studies revealed slow magnetic relaxation, placing **2** among dysprosocenium-based single-molecule magnets containing a doubly anionic ligand in the equatorial plane.

Received 21st October 2021,
Accepted 4th January 2022

DOI: 10.1039/d1qi01331a

rsc.li/frontiers-inorganic

Introduction

Multidentate Schiff base ligands, such as salen-type ligands, where salen = *N,N*′-bis(salicylidene)-ethylenediamine, form stable complexes with transition metals,[1] lanthanides,[2] and actinides,[3] comprising various metal oxidation states and featuring compounds of differing nuclearity. In particular, the *tert*-butyl-functionalized salophen ligand, *N,N*′-*o*-phenylene-bis(3,5-di-*tert*-butylsalicylidene-imine) ($H_2{}^{tBu}salophen$), has been exploited in coordination chemistry due to its facile synthesis,[4,5] multidentate nature, and redox-activity.[6] Metal-salophen complexes also undergo reversible redox processes,[5,7–10] rendering them potentially useful for catalysis in systems with redox-inactive metal centres. Furthermore, salophen-containing complexes have also been probed for applications in medicine,[11,12] luminescence,[13,14] and molecular magnetism.[15–17]

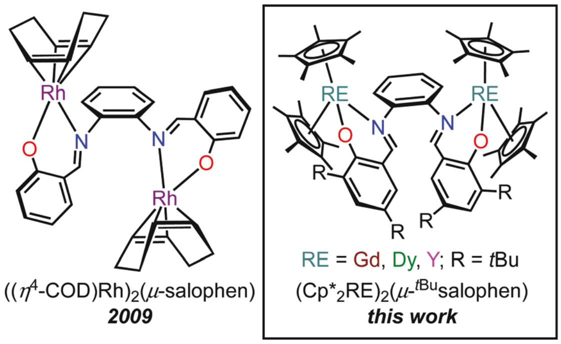

Fig. 1 Organometallic complexes featuring a bridging salophen ligand. (Left) Dirhodium 1,5-cyclooctadiene (COD) complex, $((\eta^4\text{-COD})Rh)_2(\mu\text{-salophen})$ and (right) bimetallic rare earth (RE) metallocenes, $(Cp^*_2RE)_2(\mu\text{-}^{tBu}salophen)$, RE = Gd (**1**), Dy (**2**), and Y (**3**).

Mononuclear transition metal salophen complexes typically feature an encapsulated metal ion in the *N,N,O,O*-binding pocket of the salophen ligand leaving axially accessible metal sites for applications in catalysis.[4] In contrast, employing lanthanides in salophen chemistry typically results in distinct coordination environments owing to the large ionic size of the lanthanides. The most prevalent coordination motif of salophen to lanthanide ions, results in mono- and multinuclear coordination complexes, with the lanthanide centre encapsulated between two *N,N,O,O*-coordination pockets of the salophen ligand.[5,16,18] Notably, the organometallic chemistry of salophen ligands with lanthanides is yet to be discovered, possibly due to the challenging synthesis, purification, and characterisation of organolanthanide complexes, owing to the reduced coordinative ability of the non-rigid ligand and sterically constrained metal sites dictated by two cyclopentadienyl

---

Department of Chemistry, Michigan State University, 578 South Shaw Lane, East Lansing, Michigan, 48824, USA. E-mail: sdemir@chemistry.msu.edu

† Electronic supplementary information (ESI) available: X-ray crystallographic file in the CIF format. Computational data, spectroscopic data, and detailed crystallographic information for 1, 2, and 3 are included. CCDC 2116668 (1), 2116666 (2), 2116667 (3). For ESI and crystallographic data in CIF or other electronic format see DOI: 10.1039/d1qi01331a

(Cp) units. Consequently, metallocenes comprising large bridging moieties are scarce and involve either rigid ligands without the possibility to rotate or flexible units with high coordination sites (≥six). In particular, the utilization of salophen ligands in biscyclopentadienyl lanthanide chemistry, also referred to as metallocenes, is not only fundamentally interesting but also highly desirable in the context of the development of new single-molecule magnets (SMMs). The latter bear huge potential applications in the area of high-density information storage, magnetic refrigeration, spin-based electronics, and quantum computing.[19,20] In fact, the best mono- and multinuclear SMMs in terms of highest blocking temperature and largest spin-reversal barrier thus far, are metallocene complexes comprising Cp ligands, functionalized with bulky polyalkyl and trimethylsilyl groups, respectively.[21–25] The axial ligand fields imposed by the Cp-based ligands enhances the single-ion anisotropy of the $\mathrm{Dy^{III}}$ and $\mathrm{Tb^{III}}$ ions which is pivotal in mononuclear complexes. Importantly, the combination of axial magnetic anisotropy enforced by alkyl-substituted Cp ligands with the strong magnetic exchange coupling provided by a $\mathrm{N_2}^{3-}$ radical bridge resulted in record multinuclear SMM with open magnetic hysteresis loops up to 30 K and largest coercive field (H_c = 7.9 T at 10 K) for any molecular system.[25] If the magnetic coupling to the lanthanide ion is strong enough, the implementation of such radical bridges results in suppression of quantum tunnelling of the magnetization, leading to magnetic memory effect. Despite this promising strategy, the number of radical-bridged SMMs is miniscule when contrasted to all other lanthanide-based SMMs, largely owing to the synthetic challenges of isolating and characterising such species, but also simply due to scarcity of known organometallic lanthanide complexes featuring Cp-based scaffolds and redox-active ligands bridging at least two metal centres. Hence, we are particularly interested in exploring the use of multi-dentate, redox-active ligands with the potential to bridge two or even more metals in organolanthanide chemistry.

Large aromatic organic ligands leave room for chemical tunability and potential access to multiple open shell oxidation states, allowing for correlations of various radical oxidation states and magnetic exchange. Notably, implementation of a large bridging ligand may result in important ramifications on the electronic and magnetic properties, as demonstrated with ytterbocene charge-transfer molecular wire complexes.[26] Hence, we focused on devising a route to salophen-bridged organometallic rare earth (RE) complexes with trivalent Gd, Dy, and Y. The implementation of (a) gadolinium allows for the quantification of magnetic exchange coupling owing to the near isotropic nature of $\mathrm{Gd^{III}}$ ions, (b) dysprosium potentially gives rise to SMM behaviour due to its high magnetic anisotropy originating from large unquenched orbital angular momentum and strong spin–orbit coupling and (c) yttrium facilitates NMR and computational studies due to nuclear spin $I = \frac{1}{2}$ of ^{89}Y and inherent diamagnetism.

Herein, we describe the synthesis, structural, spectroscopic, computational, and magnetic characterisation, as well the redox-behaviour of three new rare earth metallocene complexes, $(\mathrm{Cp^{*}_2RE})_2(\mu\text{-}^{t\mathrm{Bu}}\mathrm{salophen})$, where RE = Gd (**1**), Dy (**2**), and Y (**3**); Cp* = 1,2,3,4,5-pentamethylcyclopentadienyl. Importantly, these complexes represent the first crystallographically characterised salophen-bridged metallocenes eqn (1). The synthetic route to obtain **1–3** employs the well-known tetraphenylborate complexes, $\mathrm{Cp^{*}_2RE(BPh_4)}$, which readily undergo salt metathesis reactions due to the presence of a weakly coordinated tetraphenylborate anion, $(\mathrm{BPh_4})^-$.[27] These tetraphenylborate complexes are useful building blocks to access mono-,[28] di-,[29,30] and trimetallic,[31] systems bearing RE-metallocene units that are bridged through radical- and non-radical ligands. Notably, the $\mathrm{Cp^{*}_2Ln(BPh_4)}$ complexes (Ln = Nd, Tb, Dy) exhibit SMM behaviour where the axial ligand field imposed by the bis-pentamethylcyclopentadienyl scaffold is most adequate for lanthanide ions with an oblate 4f-electron density.[32,33]

Experimental section

Materials and methods

All manipulations were performed using an MBraun glovebox under a dry nitrogen atmosphere. House nitrogen was purified through an Mbraun HP-500-MO-OX gas purifier. *N*-Hexane and THF were distilled over calcium hydride and potassium, respectively. Benzophenone was used as an indicator for THF. Toluene was dried over potassium and distilled prior to use. Deuterated solvents were purchased from Cambridge Isotope Laboratories and dried over 3 Å sieves prior to use. Ethanol was purchased from Sigma Aldrich and used as received. Pentamethylcyclopentadiene (HCp*), allylmagnesium chloride (2.0 M in THF), anhydrous $\mathrm{RECl_3}$ (RE = Gd, Dy and Y), 3,5-di-*tert*-butylsalicylic acid, and *o*-phenylenediamine were purchased from Sigma Aldrich and used as received. Potassium bis(trimethylsilyl)amide (KN*) was also purchased from Sigma Aldrich, dissolved in toluene, centrifuged, and the resulting supernatant was filtered through Celite prior to crystallization from toluene at −35 °C. Potassium graphite ($\mathrm{KC_8}$),[34] potassium pentamethylcyclopentadienide (KCp*),[34] and triethylammonium tetraphenylborate $(\mathrm{HNEt_3})(\mathrm{BPh_4})$[35] were prepared according to literature procedures. $\mathrm{Cp^{*}_2RE(\mu\text{-}Cl)_2K}$, $\mathrm{Cp^{*}_2RE(\eta^3\text{-}C_3H_5)}$, and $\mathrm{Cp^{*}_2RE(BPh_4)}$, where RE = Gd, Dy and Y, were prepared according to literature procedures.[30] UV-vis spectra were collected with a PerkinElmer Lambda 1050 UV-Vis-NIR spectrophotometer at ambient temperature from 250 to 750 nm. Samples were prepared in a dry argon-filled glove box and measured in a 1 cm quartz cuvette, outfitted with a Teflon screw cap. The spectra were baseline corrected from a sample of dry and filtered THF. IR spectra were recorded with an Agilent Cary 630 FTIR spectrometer on crushed crystalline solids in a nitrogen-filled glovebox. Elemental analysis (EA) was performed at Michigan State University, using a PerkinElmer 2400 Series II CHNS/O analyser. Crystalline sample materials were heated to

60 °C under vacuum for 5 h in order to ensure complete desolvation prior to EA measurement. Frozen solution X-band EPR were recorded on a Bruker Elexsys E-680X at 10 K in Young quartz EPR tubes using thoroughly dried solvent (THF). Simulation of the spectrum was attempted by using the EasySpin software package[36] for MATLAB.

Synthesis of $H_2{}^{tBu}$salophen. $H_2{}^{tBu}$salophen was synthesized from a modified literature procedure under ambient conditions.[4] A 10 mL ethanol solution of 3,5-di-*tert*-butylsalicylicaldehyde (6.9284 g, 0.030 mol, 2 equiv.) was added to a 250 mL round bottom flask containing a stirring 5 mL ethanol solution of *o*-phenylenediamine (1.5990 g, 0.015 mol, 1 equiv.). An additional 20 mL of ethanol was added and refluxed at 85 °C overnight. The cloudy dark orange solution was allowed to cool to room temperature before being cooled further over dry ice for 30 min prior to vacuum filtration, yielding a yellow-orange solid. Residual water was removed under dynamic vacuum and heat. Yield: 6.7828 g, 0.013 mol, 85%. ^{1}H NMR (500 MHz, C_6D_6, Fig. S4, ESI†) δ 14.04 (s, 2H, (C_6H_2)-O*H*), 8.12 (s, 2H, N═C*H*), 7.63 (d, $^4J_{H-H}$ = 2.4 Hz, 2H, *p-H* (C_6H_2)), 7.05 (d, $^4J_{H-H}$ = 2.4 Hz, 2H, *o-H* (C_6H_2), 6.99 (dd, $^3J_{H-H}$ = 5.9, 3.4 Hz, 2H, *m*-C*H* (C_6H_4)), 6.73 (dd, $^3J_{H-H}$ = 5.9, 3.4 Hz, 2H, *o*-C*H* (C_6H_4)), 1.66 (s, 18H, C*Me*$_3$), 1.34 (s, 18H, C*Me*$_3$). See NMR section for details.

Synthesis of $K_2{}^{tBu}$salophen. $K_2{}^{tBu}$salophen was synthesized from a modified literature procedure.[5] In a 20 mL vial, potassium bis(trimethylsilyl)amide (0.2932 g, 1.470 mmol, 2.15 equiv.) was dissolved in 5 mL of toluene and added dropwise to a stirring 10 mL toluene solution of ^{tBu}salophen (0.3697 g, 0.684 mmol, 1 equiv.). An immediate formation of insoluble orange solids was observed, after which the orange suspension was allowed to stir for 15 min. Volatiles and solvent were removed under vacuum and the orange solids were washed with *n*-hexane before drying under dynamic vacuum. Yield: 0.3570 g, 0.579 mmol, 85%. ^{1}H NMR (500 MHz, C_6D_6, Fig. S4, ESI†) δ 8.49 (s, 2H, N═C*H*), 7.65 (d, $^4J_{H-H}$ = 2.8 Hz, 2H, *p*-C*H* (C_6H_2)), 7.26 (d, $^4J_{H-H}$ = 2.8 Hz, 2H, *o*-C*H* (C_6H_4)), 1.78 (s, 18H, C*Me*$_3$), 1.49 (s, 18H, C*Me*$_3$).

Synthesis of $(Cp^*{}_2Gd)_2(\mu\text{-}{}^{tBu}$salophen), 1. A 2 mL solution of $K_2{}^{tBu}$salophen (63.9 mg, 0.104 mmol, 1 equiv.) was added dropwise to a stirring 5 mL THF solution of $Cp^*{}_2Gd(BPh_4)$ (155.8 mg, 0.207 mmol, 2 equiv.) and was stirred at room temperature for 3 h. An immediate color change from a pale clear solution to dark red was observed. A gradual precipitation of a colorless insoluble solid, presumably potassium tetraphenylborate, was observed within 10 min. The insoluble solids were removed by filtration and the resulting red filtrate was evaporated to dryness to afford a red solid. The product was extracted with *n*-hexane, filtered, and the resulting red filtrate was evaporated to dryness. Red block-shaped crystals suitable for X-ray analysis were grown from a concentrated toluene solution at −35 °C within 3 d. Crystalline yield: 69.5 mg, 0.050 mmol, 48%. Anal. Calc. for $C_{76}H_{106}Gd_2N_2O_2$: C, 65.47; H, 7.66; N, 2.01. Found: C, 65.12; H, 7.43; N, 1.93. IR spectrum (cm^{-1}, Fig. S17, ESI†): 2902w, 1579s, 1526s, 1415s, 1321m, 1254m, 1155s, 1001m, 889m, 839m, 786m, 755m. Due to the paramagnetic nature of **1**, no signals were observed in the ^{1}H NMR spectrum.

Synthesis of $(Cp^*{}_2Dy)_2(\mu\text{-}{}^{tBu}$salophen), 2. The synthesis of **2** was performed employing the same procedure as described for **1**, using $Cp^*{}_2Dy(BPh_4)$ (92.2 mg, 0.123 mmol, 2 equiv.) and $K_2{}^{tBu}$salophen (37.8 mg, 0.061 mmol, 1 equiv.). Red block-shaped crystals of **2** suitable for X-ray analysis were grown from a concentrated toluene solution at −35 °C within 3 d. Crystalline yield: 54.1 mg, 0.039 mmol, 63%. Anal. Calc. for $C_{76}H_{106}Dy_2N_2O_2$: C, 64.98; H, 7.61; N, 1.99. Found: C, 65.08; H, 7.82; N, 1.90. IR spectrum (cm^{-1}, Fig. S18, ESI†): 2902w, 1579s, 1526s, 1413s, 1321m, 1256m, 1155s, 1001m, 889m, 837m, 788m, 755m, 726s, 693m. ^{1}H NMR (500 MHz, C_6D_6) δ 84.98, 77.69, 7.32, 7.00, 1.18, 0.82, −32.09 (br), −51.20 (br), −100.75.

Synthesis of $(Cp^*{}_2Y)_2(\mu\text{-}{}^{tBu}$salophen), 3. The synthesis of **3** was performed employing the same procedure as described for **1**, using $Cp^*{}_2Y(BPh_4)$ (100.6 mg, 0.148 mmol, 2 equiv.) and $K_2{}^{tBu}$salophen (44.6 mg, 0.072 mmol, 1 equiv.). Red block-shaped crystals of **3** suitable for X-ray analysis were grown from a concentrated toluene solution at −35 °C within 3 d. Crystalline yield: 68.1 mg 0.054 mmol, 73%. Anal. Calc. for $C_{76}H_{106}Y_2N_2O_2$: C, 72.59; H, 8.50; N, 2.23. Found: C, 73.04; H, 8.54; N, 2.11. IR spectrum (cm^{-1}, Fig. S19, ESI†): 2890w, 1579s, 1526s, 1412s, 1319m, 1256m, 1155s, 1001m, 889m, 837m, 786m, 755m, 726s, 693m. ^{1}H NMR (800 MHz, C_6D_6) δ 8.88 (d, $^3J_{Y-H}$ = 2.2 Hz, 2H, N═C*H*), 7.51 (d, $^4J_{H-H}$ = 2.6 Hz, 2H, *p*-C*H* (C_6H_2)), 7.10 (dd, $^3J_{H-H}$ = 5.8, 3.4 Hz, 2H, *m*-C*H* (C_6H_4)), 6.92 (d, $^4J_{H-H}$ = 2.6 Hz, 2H, *o*-C*H* (C_6H_2)), 6.65 (dd,$^3J_{H-H}$ = 5.8, 3.4 Hz, 2H, *o*-C*H* (C_6H_4)), 2.06 (s, 30H, C_5*Me*$_5$), 1.86 (s, 30H, C_5*Me*$_5$), 1.72 (s, 18H, C*Me*$_3$), 1.14 (s, 18H, C*Me*$_3$).^{13}C NMR (201 MHz, C_6D_6) δ 174.32 (N═*C*H), 168.29 ((C_6H_2)*C*–O), 141.47 ((C_6H_4)*C*–N), 139.59 ((C_6H_2)*C*-CMe$_3$), 137.37 ((C_6H_2)*C*-CMe$_3$), 132.73 (*p*-*C*H (C_6H_2)), 130.70 (*o*-*C*H (C_6H_2)), 128.35 (*m*-*C*H (C_6H_4)), 127.11 (*o*-*C*H (C_6H_4)), 122.14 ((C_6H_2)*C*-CH), 118.52 (*C*$_5$Me$_5$), 118.23 (*C*$_5$Me$_5$), 35.95 (*C*Me$_3$), 34.04 (*C*Me$_3$), 31.40 (C*Me*$_3$), 31.00 (C*Me*$_3$), 11.99 (C_5*Me*$_5$), 11.76 (C_5*Me*$_5$). ^{89}Y NMR (24.5 MHz, C_6D_6) δ −151.92 (d, $^3J_{Y-H}$ = 2.2 Hz, N═C*H*). ^{89}Y-{^{1}H} (24.5 MHz, C_6D_6) δ −151.90 (s).

X-ray crystallography. Dark red block-shaped crystals were mounted on a nylon loop with paratone oil. Data were collected using a XtaLAB Synergy, Dualflex, HyPix diffractometer equipped with an Oxford Cryosystems low-temperature device, operating at T = 100.00(10) K. Data were measured using w and f of 0.5° per frame for 0.1 s using Mo K$_\alpha$ radiation (micro-focus sealed X-ray tube, 50 kV, 1 mA). The total number of runs and images was based on the strategy calculation from the program CrysAlisPro 1.171.40.74a (Rigaku OD, 2020). Cell parameters were retrieved using the CrysAlisPro 1.171.40.74a (Rigaku OD, 2020) software and refined using CrysAlisPro 1.171.40.74a (Rigaku OD, 2020). Data reduction was performed using the CrysAlisPro 1.171.40.74a (Rigaku OD, 2020) software which corrects for Lorentz polarization. Correction for absorption effects was done using a numerical correction based on Gaussian integration over a multifaceted crystal model and an empirical correction using spherical harmonics, implemented

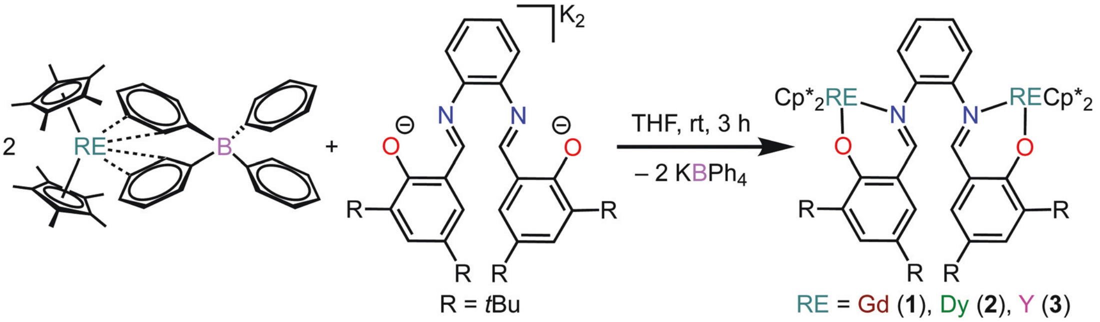

(**1**)

in SCALE3 ABSPACK scaling algorithm (spherical harmonics and frame scaling). The structure was solved in the space group $P\bar{1}$ by using intrinsic phasing, using the ShelXT[37] 2018/2 (Sheldrick, 2018) structure solution program. The structure was refined by least-squares ShelXL[38] incorporated in Olex2 software program.[39] All non-hydrogen atoms were refined anisotropically. Hydrogen atom positions were calculated geometrically and refined using the riding model, except for the hydrogen atom on the non-carbon atom(s) which were found by difference Fourier methods and refined isotropically when data permitted.

^{1}H, ^{13}C, and ^{89}Y NMR spectroscopy. ^{1}H and ^{13}C NMR spectra were recorded on a 500 MHz Agilent DirectDrive2 500 and a Bruker Avance III HD 800 MHz spectrometer with a TCI CryoProbe and calibrated to the residual solvent signals (C_6D_6: δ_H = 7.16 ppm). Signal multiplicities are abbreviated as: s (singlet), d (doublet), m (multiplet), br (broad). Chemical shift assignments were denoted using the following abbreviations: *o* (ortho), *m* (meta), *p* (para), and Me (methyl). Air-sensitive samples were prepared in a nitrogen-filled glovebox and sealed air-tight.

^{89}Y NMR measurements were performed with a Varian Inova-500 NMR spectrometer, using a 5 mm diameter J. Young NMR tube containing a 20 mmol solution of $(Cp^*_2Y)_2(\mu\text{-}^{tBu}\text{salophen})$, **3**, in C_6D_6. The chemical shifts were referenced to a sample of 3 M YCl_3 in D_2O. The reference solution was filtered into a capillary, flame-sealed, and added to the 20 mmol solution of **3** prior to measurement. Due to the long relaxation times reported for ^{89}Y,[40–42] pulse delays were set to 60 s and pulsed at an angle of 30°. Data acquisition times were set to 1 and 2 s for inverse gated proton-decoupled yttrium-89 (^{89}Y-{^{1}H}) and yttrium-89 NMR experiments, respectively. Thus, each ^{89}Y NMR experiment was conducted over 36 h at 25 °C.

Magnetic susceptibility measurement. Magnetic samples of **1** and **2** were prepared by addition of molten eicosane (at 60 °C) to crushed polycrystalline material. The eicosane served to saturate and cover the samples to prevent crystallite torquing and provide good thermal contact between the sample and the bath.

After ensuring an air-tight seal, the samples were transferred out of the glovebox and mounted onto the SQUID sample holder. Magnetic susceptibility measurements were performed with a Quantum Design MPMS3 SQUID magnetometer. Dc magnetic susceptibility data were collected at temperatures ranging from 2 to 300 K using applied fields of 0.5 and 1 T. Ac magnetic susceptibility data were collected under a 3 Oe switching field and 1000 Oe applied dc field. All data were corrected by taking into account diamagnetic contributions from the eicosane, and core diamagnetism determined by employing Pascal constants.[43] Cole–Cole plots were fitted employing formulae describing χ' and χ'' with regard to frequency, constant temperature susceptibility (χ_T), adiabatic susceptibility (χ_S), relaxation time (τ), and a variable constituting the distribution of relaxation times (α).[44] All data were fitted to α values of ≤ 0.09.

Computational methods. All density functional theory (DFT) calculations were performed with the Gaussian 16 software package.[45] To determine a suitable method for the characterisation of **3**, three functionals and four basis sets were tested and **3** was calculated as a neutral singlet. In addition, all calculations included Grimme's D3 dispersion correction.[46]

Beginning from the crystallographic coordinates of **3**, geometry optimizations were done using the hybrid B3LYP[47] and TPSSh[48] functionals, as well as the pure DFT functional, TPSS.[49] Four basis set combinations were tested comprising (1) the split valence def2-SV(P)[50,51] basis set on all atoms, with polarization functions on heavy atoms, including the intrinsic 28 in-core electrons effective core potential for Y atoms, (2) a def2-SV(P)[50,51] atomic orbital description for Y atoms, and the 6-31G(d,p)[52–54] basis set for O, N, C, and H atoms, (3) a def2-SV(P)[50,51] basis set for Y atoms, and the 6-31+G(d, p)[52–55] basis set for O, N, C, and H atoms, (4) the valence triple zeta def2-TZVP[50,51] basis set and intrinsic 28 in-core electrons pseudopotential for Y atoms, and 6-311G(d,p)[55,56] basis set for O, N, C, and H atoms. A statical analysis of the optimized geometries was performed considering the mean absolute deviation (MAD), mean squared error (MSE), root mean squared error (RMSE), and mean absolute percentage error (MAPE) (Tables S4–S6, ESI†). Here, the TPSSh functional, in conjunction with the def2-SV(P)&6-311G(d,p) basis sets was found to be in excellent agreement with the experimental crystallographic distances and angles. Thus, the TPSSh/def2-TZVP&6-311G(d,p) method was used for all subsequent DFT calculations, including the analytical frequency calculations to confirm that the stationary points are indeed local minima.

Results and discussion

Structural analysis

1–3 were synthesized by reacting $\mathrm{Cp^*_2RE(BPh_4)}$ with $\mathrm{K_2}$$^{t\mathrm{Bu}}$salophen in THF, eqn (1). Crystallisation from concentrated toluene solutions at −35 °C gave red block-shaped crystalline solids suitable for single crystal X-ray analysis over the course of three days in 48%, 63%, and 73% yield for **1**, **2**, and **3**, respectively. Compounds **1–3** are isostructural (Table S1, ESI†), crystallizing in the $P\bar{1}$ space group, with three co-crystallised toluene molecules in the crystal lattice. Each metal ion is coordinated by an *N*,*O*,-bound ($^{t\mathrm{Bu}}$salophen)$^{2-}$ ligand and two (η^5-Cp*)$^-$ ligands in an eight-coordinate, distorted see-saw geometry (Fig. 2 and S1–S3, ESI†). Thus, **1–3** constitute the first crystallographically characterised salophen-bridged metallocene complexes for any metal, for which a bimetallic six-coordinate rhodium COD complex (COD = 1,5-cyclooctadiene), ((η^4-COD)Rh)$_2$(μ-salophen),[57] serves as the closest analogue (Fig. 1). In addition, **1** and **2** simultaneously serve as the first organometallic f-element salophen complexes. For **2**, the average M–Cnt (where Cnt = Cp* ring centroid) distance is 2.405(1) Å, and the average Cnt–M–Cnt angle is 135.9(1)°, slightly exceeding the respective angle of 134.0° observed in $\mathrm{Cp^*_2Dy(BPh_4)}$.[59] Furthermore, the Dy–O distances of 2.183(3) Å and 2.190(4) Å are in the range of 2.181(10)–2.444(11) Å for dysprosium salophen sandwich complexes, as well as Dy–O$_{\mathrm{alkoxide}}$ distances in $\mathrm{[Dy(OCPh_3)_2(THF)_4](BPh_4)}$.[58] Similarly, the Dy–N distances of 2.484(2) Å and 2.452(3) Å are in agreement with comparable Dy–N distances of neutral N-donor ligands that are coordinating to Dy.[59] The average N–RE–O angle of 75.8(1)° is slightly smaller than 78.4° found in the less sterically congested indigo-bridged Dy complex, $\mathrm{(Cp^*_2Dy)_2}$(μ-indigo),[60] which also contains a six-membered heterocyclic ring. Overall, the shrinkage of metal–ligand donor atom distances traversing from Gd$^{\mathrm{III}}$ to Dy$^{\mathrm{III}}$ to Y$^{\mathrm{III}}$ is consistent with the gradual decrease in ionic radii of the trivalent RE ions.[61] In addition, the intramolecular M⋯M distances also drop from 7.895(1) Å to 7.872(2) Å to 7.858(1) Å traversing from **1** to **2** to **3**, respectively.

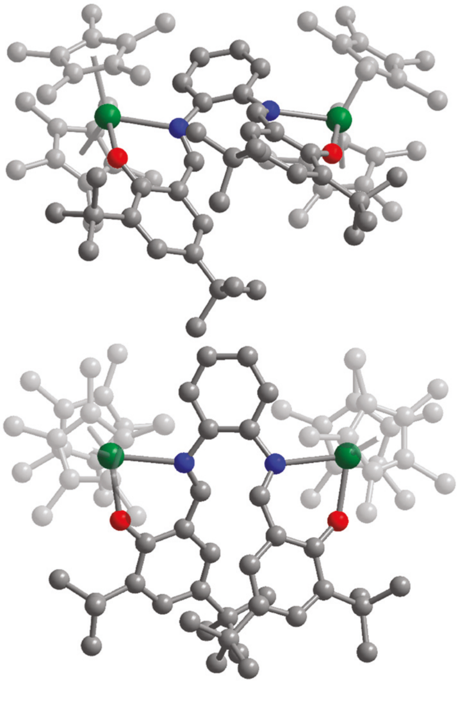

Fig. 2 Structure of $\mathrm{(Cp^*_2Dy)_2}$(μ-$^{t\mathrm{Bu}}$salophen), **2**. (Top) Front perspective and (bottom) arial perspective. Green, red, blue, and grey spheres represent Dy, O, N, and C atoms, respectively. (Cp*)$^-$ ligands have been faded for clarity. Hydrogen atoms, and solvent molecules in the crystal lattice, have been omitted for clarity. Selected distances (Å) and angles (°): M–Cnt: 2.439(1) (**1**), 2.405(1) (**2**), 2.403(1) (**3**); M–N: 2.484(2)/2.452(3) (**1**), 2.454(4)/2.457(4) (**2**), 2.447(2)/2.452(2) (**3**); M–O: 2.207(2)/2.217(2) (**1**), 2.183(3)/2.190(4) (**2**), 2.168(2)/2.176(2) (**3**); M⋯M: 7.895(1) (**1**), 7.872(1) (**2**), 7.858(1) (**3**); Cnt–M–Cnt: 135.7(1) (**1**), 135.9(1) (**2**), 137.0(1) (**3**); N–M–O: 75.4(1)/73.5(1) (**1**), 76.1(1)/75.4(1) (**2**), 76.5/75.7(1) (**3**). Cnt = Cp* ring centroid.

Solution state properties

The solution state structures of **1–3** were investigated by ^{1}H and ^{13}C NMR (Fig. S5–S7 and S10, ESI†), as well as UV-Vis-NIR spectroscopy (Fig. 4, top). For the analogues containing paramagnetic lanthanides, the signals of the ^{1}H NMR could not be ascribed. For **1**, the proton spectrum was featureless, while **2** exhibited both broad and sharp peaks between 100 and −100 ppm, which could not be assigned. For the diamagnetic Y congener, **3**, the proton and carbon peaks could be readily assigned in both the 1D and 2D NMR spectra (Fig. S7–S13, ESI†). The 100% natural abundance and $I = \frac{1}{2}$ of the ^{89}Y isotope enabled further structural characterisation *via* ^{89}Y NMR spectroscopy. The long T_1 relaxation times of the ^{89}Y isotope require extended data acquisition times or signal enhancement through dynamic nuclear polarization.[62] Therefore, 20 mmol solutions of **3** were measured in the presence of a 3 M $\mathrm{YCl_3}$ in $\mathrm{D_2O}$ external standard using a 30° pulse angle and relaxation delays of 60 s over the course of 36 h. In addition, inverse gated proton-decoupled ^{89}Y (^{89}Y-{^{1}H}) and ^{89}Y NMR experiments were undertaken to probe the presence of Y–H coupling, where such couplings may occur in yttrium metallocenes, such as confirmed for [Cp$^{\mathrm{Me}}$$_2$Y(μ-H)(THF)]$_2$ and {[Cp$_2$Y(μ-H)$_3$](μ$_3$-H)}$^-$.[63] The proton-coupled ^{89}Y NMR spectrum of **3** exhibited a broad doublet at approximately −151.9 ppm (Fig. S14 and S15, ESI†), which coalesced to a sharp singlet in the proton-decoupled ^{89}Y spectrum (Fig. 3). This significant

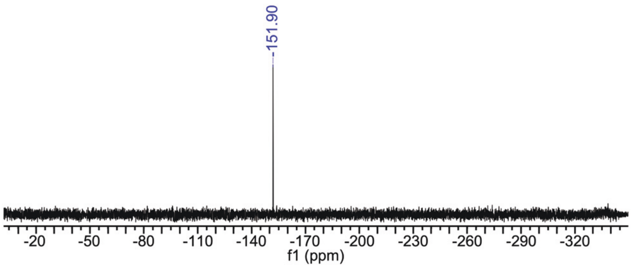

Fig. 3 Proton-decoupled ^{89}Y NMR (^{89}Y-{^{1}H}) (20 mmol, 24.5 MHz, $\mathrm{C_6D_6}$, 25 °C) spectrum of $\mathrm{(Cp^*_2Y)_2}$(μ-$^{t\mathrm{Bu}}$salophen), **3**, measured from −1 ppm to −350 ppm. ^{89}Y NMR signal is referenced to a 3 M solution of $\mathrm{YCl_3}$ in $\mathrm{D_2O}$.

line broadening observed in the absence of proton-decoupling suggests the possibility of Y–H coupling. In fact, a 2.2 Hz coupling constant in the ^{89}Y NMR spectrum was deconvoluted through the implementation of a Lorentzian–Gaussian fit, as implemented in MestReNova V. 14.1.1, and is consistent with the 2.2 Hz coupling constant calculated for the doublet of the imine group in **3** (Fig. S7, ESI†). Furthermore, the absence of off-diagonal peaks in the 2D ^{1}H–^{1}H COSY (Fig. S8 and S9, ESI†) of **3** suggests that the doublet feature is not a consequence of proton-proton coupling. Thus, these doublet feature in the ^{1}H and ^{89}Y spectra can be ascribed to the presence of $^{3}J_{\text{Y–H}}$ coupling. Characterisation of ^{89}Y chemical shifts on Cp*-based systems are still rare,[64] possibly due to elaborate exposure times and the challenge of handling air-sensitive compounds for an extended period of time, rendering comparative studies even scarcer. Here, the chemical shift monitored for the ^{89}Y spectrum of **3** appears upfield when contrasted to −129.3 ppm recorded for the structurally closest yttrium metallocene complex, $Cp^*_2Y(OAr)$ where OAr = *o*-2,6-$((CH_3)_3C)_2C_6H_3$, albeit mononuclear.[65]

The electronic absorption spectra of **1–3** all exhibit similar absorption features, with strong ligand-centred π–π* and n–π* transitions in the near-UV-visible spectral region.[14,18] In fact, for **3**, the shoulder and sharp transition at approximately 3.8 × 10^4 cm^{-1} and 3.3 × 10^4 cm^{-1}, respectively, are ascribed to π–π* transitions originating from the imino moieties of the bridging salophen ligand.[14,18] Furthermore, the broad absorption features near 2.5 × 10^4 cm^{-1} and 2.1 × 10^4 cm^{-1} are attributed to the n–π* transitions arising from the non-bonding electrons of the phenolate groups of the salophen ligand. These ligand-centred transitions are congruent with lanthanide-salophen complexes.[14,18]

The redox activity of **1–3** was investigated *via* cyclic voltammetry to probe whether oxidation state changes on the central salophen ligand may be observable on the time scale of the electrochemical experiment. Thus, cyclic voltammetry was performed in THF using $(^n\text{Bu}_4\text{N})(\text{PF}_6)$ as an electrolyte. Here, a quasi-reversible feature was observed at −1.5, −1.4, and −1.2 V *versus* [Fc]/[Fc$^+$] for **1**, **2**, and **3**, respectively (Fig. 4 bottom and S28, ESI†), suggestive of an accessible open shell salophen$^{3-\bullet}$-bridged complex.[10] This paves the way for chemical studies regarding accessibility of radical-bridged variants of **1–3**.

Magnetic properties

The temperature-dependent dc molar magnetic susceptibilities of **1** and **2** were measured on polycrystalline samples under an applied magnetic field of 0.5 and 1.0 T from 2 to 300 K (Fig. 5, S20, and S21, ESI†). Under a dc field of 1.0 T, the room temperature $\chi_M T$ values for **1** and **2** are 16.08 cm^3 K mol^{-1} and 28.26 cm^3 K mol^{-1} which are in excellent agreement with the presence of two uncoupled trivalent lanthanide ions (Gd$^{\text{III}}$: $^8S_{7/2}$, $S = 7/2$, $L = 0$, $J = 7/2$, $g = 2$, $\chi_M T_{\text{calc}} = 15.76$ cm^3 K mol^{-1}; Dy$^{\text{III}}$: $^6H_{15/2}$, $S = 5/2$, $L = 5$, $J = 15/2$, $g = 4/3$, $\chi_M T_{\text{calc}} = 28.34$ cm^3 K mol^{-1}). For **1**, a steady decrease in $\chi_M T$ to 15.51 cm^3 K mol^{-1} at 12 K is observed before declining rapidly to 11.04 cm^3 K mol^{-1} at 2 K. This behaviour is typically associated with the

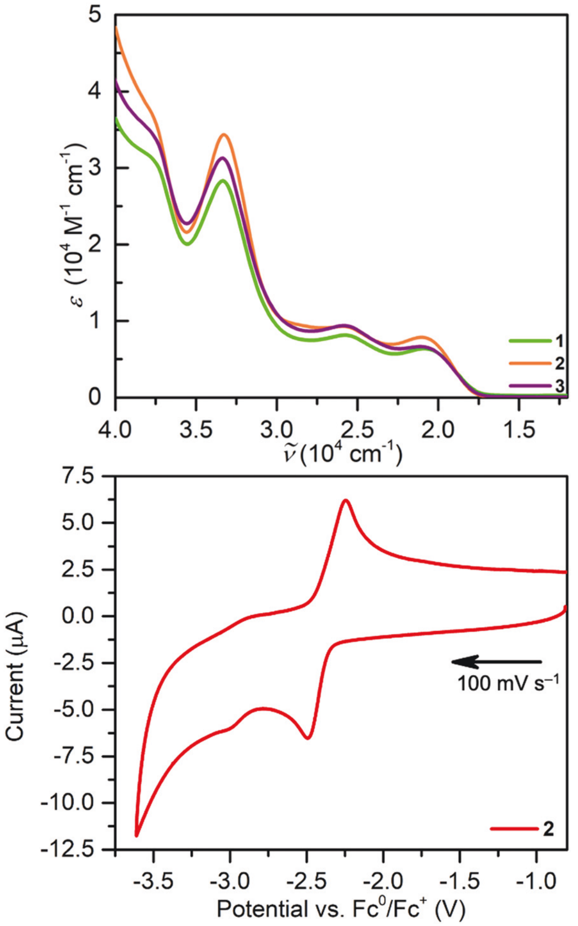

Fig. 4 (Top) UV-Vis-NIR spectra $(Cp^*_2RE)_2(\mu\text{-}^{tBu}\text{salophen})$, where RE = Gd (**1**), Dy (**2**), and Y (**3**) in THF. (Bottom) Cyclic voltammogram of **2** in 1 mM $(^n\text{Bu}_4\text{N})(\text{PF}_6)$ THF solution at 100 mV s^{-1} scan rate.

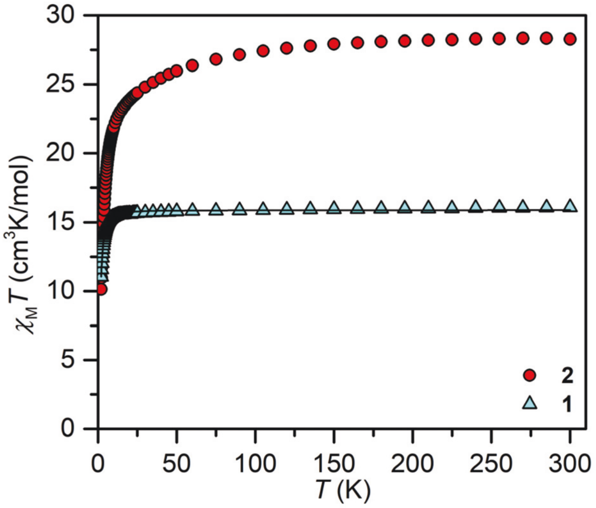

Fig. 5 Plots of $\chi_M T$ *vs.* *T* for $(Cp^*_2Gd)_2(\mu\text{-}^{tBu}\text{salophen})$, **1** (blue triangles), and $(Cp^*_2Dy)_2(\mu\text{-}^{tBu}\text{salophen})$, **2** (red circles), between 2 and 300 K under a dc field of 1.0 T. The black line represents the best fit of the data for **1**.

depopulation of low-lying excited states. The $\chi_M T(\mathrm{T})$ data for **1** were fit with PHI[66] (Table S2, ESI†), which employs the spin Hamiltonian $\hat{H} = -2J\hat{S}_{Gd}\hat{S}_{Gd}$, and yielded a magnetic exchange coupling constant, J, and g values of −0.0053(4) cm^{-1} and 2.0077(7), respectively, at 1.0 T. Compared to other dinuclear bismetallocenes (Table S3†), the quantified coupling strength is weak, which is, however, expected, given the size of the diamagnetic bridge. For **2**, a similar trend is monitored at 1.0 T in the temperature dependence of the product of magnetic susceptibility and temperature, where a gradual drop in $\chi_M T$ to 21.87 cm^3 K mol^{-1} at 10 K is observed which is followed by a sharp decrease to 10.13 cm^3 K mol^{-1} at 2 K, indicative of a depopulation of low-lying excited states.[44]

Field-dependent magnetization data for **1** and **2** were recorded from 0 to 7 T between 1.8 and 10 K, (Fig. S22 and S23, ESI†). At 1.8 and 2 K, a rapid rise in magnetization was observed for **2** at lower fields, while measurements at higher temperature saturated slowly due to the substantial magnetic anisotropy of the Dy^{III} ions and/or antiferromagnetic coupling between the metal ions.[67] The maximum magnetic moment at 1.8 K (10.81 $N\mu_B$) is in good agreement with the expected value for two uncoupled Dy^{III} ions (2 × 5.23 $N\mu_B$) in an environment affected by crystal field effects.[68–70] This is also reflected in the reduced magnetization plots (*M vs. H/T*, Fig. S23, ESI†) where curves do not superimpose to a single curve, which is typically attributed to significant magnetic anisotropy and/or the presence of low-lying excited states.[71–73] For **1** in contrast, the *M vs. H/T* plots superimpose well between 1.8 and 10 K, indicative of negligible magnetic anisotropy and therefore, very small zero-field splitting (Fig. S22, ESI†). In principle, the observed downturn in $\chi_M T$ plots may also be attributed to the apparent weak magnetic exchange coupling between the lanthanide ions. The influence of small magnetic coupling in dinuclear Gd^{III} complexes may be investigated through electron paramagnetic resonance (EPR) spectroscopy, where through simulation of the collected spectra the influence of J and the zero field parameters D and E may be analysed in greater detail.[71] For mononuclear Gd^{III} complexes the zero-field splitting parameters, obtained through EPR spectroscopy, are within 0.016–0.061 cm^{-1} (D) and 0.0046–0.017 cm^{-1} (E),[72] and thus, close in magnitude to the J value determined from magnetometry for **1**. Therefore, small variations of J are expected to dramatically influence the EPR spectrum of **1**. To quantify the coupling between the Gd^{III} ions of **1** and their zero field splitting parameters more accurately, we conducted X-band frozen THF solution EPR measurements at 10 K. The obtained broad spectra (between 2 and 7.5 × 10^3 G, Fig. S29, ESI†) showed a complex pattern of splittings likely originating from (anisotropic) hyperfine and exchange coupling, as well as zero field splitting. However, the multitude of parameters precluded a satisfactory simulation.

To probe the magnetization dynamics of **2**, ac magnetic susceptibility measurements were performed between 0.1 and 1000 Hz at low temperatures. However, no out-of-phase (χ_M'') signals were observed under a zero Oe dc field. The lack of zero field slow magnetic relaxation may be ascribed to the presence of substantial quantum tunnelling of the magnetization (QTM), possibly stemming from the strong transverse anisotropy imposed by the equatorially binding salophen ligand to each metal centre. Dysprosocenium scaffolds are inherently supported by the two axially coordinating Cp ligands which increases the single-ion anisotropy of the Dy centre.[74] However, strongly equatorially binding ligands to the dysprosocenium entity typically enhances the magnetic relaxation stemming from unfavourable strong transverse anisotropy.[75] This influence has been analysed before and was correlated with reduced axiality of the magnetic easy axis and increased mixing of ground and excited states,[75,76] while relaxation seems to be amplified through negative charges on the equatorially binding ligand. An effective way to suppress QTM is to apply a dc field.[77] Applied dc fields ranging from 500 to 2000 Oe emerged an out-of-phase (χ_M'') peak which changed intensity as a function of field strength where the optimum field was found to be 1000 Oe (Fig. S24, ESI†). Thus, ac magnetic susceptibility measurements were performed under the optimum 1000 Oe dc field, which gave rise to in-phase (χ_M') and out-of-phase (χ_M'') components of the ac magnetic susceptibility between 1.8 and 4.2 K (Fig. 6, top and middle).[78] The peak maxima of χ_M'' are moving over the entire probed temperature range. The quantitative analysis of the obtained magnetic relaxation times (τ) proceeded through the construction of Cole–Cole plots (Fig. S25, ESI†) for each temperature, which were subsequently fit to a generalized Debye model. The extracted relaxation times were used to generate an Arrhenius plot (Fig. 6, bottom). The plot curvature suggests the presence of multiple magnetic relaxation pathways. Thus, multiple fits were performed including Raman and Orbach processes alone, as well as their sum, (Fig. S26, ESI†). The inclusion of a direct process did not improve the quality of the fit and hence, was excluded. Fitting only the high temperature data (3.3 to 4.2 K) to an Orbach process afforded an effective spin-reversal barrier of U_{eff} = 8.9(4) cm^{-1} and a pre-exponential factor of τ_0 = 1.3(2) × 10^{-5} s, (Fig. S26A, ESI†). When the data was fitted over the entire probed temperature range from 1.8 to 4.2 K the barrier to spin relaxation was marginally smaller with U_{eff} = 7.8(2) cm^{-1} and an attempt time of τ_0 = 2.3(2) × 10^{-5} s (Fig. S26B, ESI†). The large τ_0 value implies that the origin of relaxation is possibly in virtue of simultaneous emission and absorption of energy rather than through an actual excited state, which interpretation is additionally supported by the more pronounced curvature at low temperatures. Thus, to explore the possibility of such a relaxation pathway, the τ values were fitted to a power law representing a Raman process only (Fig. 6, bottom). The satisfactory fit over the entire temperature range suggests that the magnetic moment at these temperatures likely relaxes *via* a Raman process. The combination of an Orbach process with the Raman process yielded U_{eff} of 12.91(5) cm^{-1} and τ_0 = 4.2(1) × 10^{-5} s, but did not alter the parameters for C and n substantially (Fig. S26C–S26D, ESI†). The moderate spin-reversal barrier and the large τ_0 value indicate that the actual barrier is much larger but not accessible through SQUID magnetometry owing to frequency range limit-

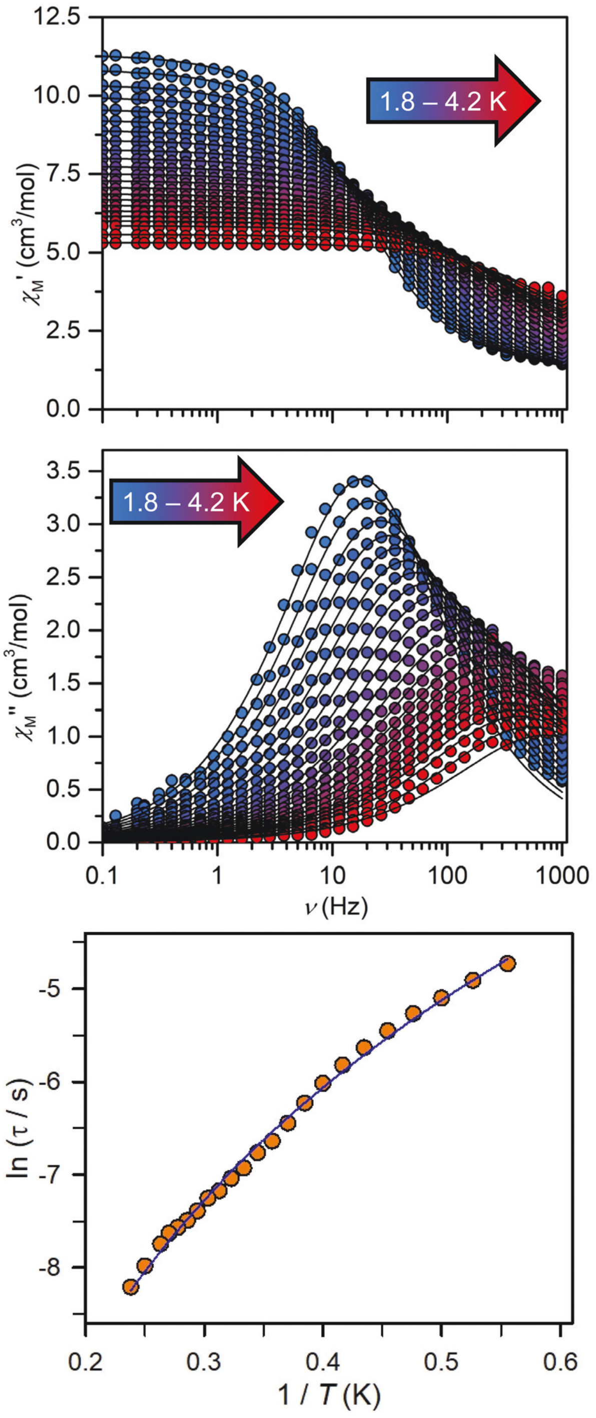

Fig. 6 (Top) In-phase (χ_M', top) and out-of-phase (χ_M'', middle) components of the ac magnetic susceptibility for $(Cp^*{}_2Dy)_2(\mu\text{-}^{tBu}\text{salophen})$, **2**, under a 1000 Oe dc field from 1.8 (blue) to 4.2 K (red). Solid lines represent fits to the data.[19] (Bottom) Arrhenius plot of relaxation time data for **2**. The solid blue line represents the fit to a Raman relaxation process affording C = 9.07 s^{-1} K^{-n}, n = 4.21.

ations. Given the intricacy of relaxation pathways,[79,80] with the data on hand, we conclude that the relaxation times are most precisely described by considering solely a Raman mechanism. In accordance with the dynamic magnetic susceptibility data, the variable-field hysteresis measurements afforded a closed magnetic hysteresis at 1.8 K (Fig. S27, ESI†).

The moderate U_{eff} values, large τ_0 values and the closed magnetic hysteresis loop point towards the absence of a pure Ising-type-limit ground state ($|\pm 15/2\rangle$) due to the admixture of excited states, thereby providing additional relaxation pathways aside from the desirable Orbach process. Studies on dinuclear metallocene Dy complexes highlighted the influence of hard equatorial ligand donor atoms,[75] and potential exchange coupling pathways through the bridging ligand, where both factors may dramatically disturb the Dy^{III} single ion anisotropy causing fast magnetic relaxation.[73] For **2**, the lower Dy^{III} single-ion anisotropy likely arises from deviation of idealized axiality provided by the bis-pentamethylcyclopentadienyl framework (compared Cnt–Ln–Cnt 135° *vs.* 180° for perfect linear) and the strong interactions of the Dy ions with two hard donors (O, N) in the equatorial plane engendering strong transverse anisotropy. The weak antiferromagnetic coupling through the salophen bridge cannot counterbalance the transverse anisotropy. Boosting the magnetic exchange through the insertion of an unpaired spin onto the salophen-bridge has great potential to mitigate these fast relaxation pathways arising from transverse anisotropy, as has been demonstrated for other radical-bridged SMMs.[81]

Computational insight

The yttrium congener, $(Cp^*{}_2Y)_2(\mu\text{-}^{tBu}\text{salophen})$, **3**, possessing diamagnetic metal centres, offers a valuable platform to further elucidate the electronic structure by computational means. Hence, DFT calculations were performed where **3** was optimized as an uncharged singlet using the hybrid functionals, B3LYP[47] and TPSSh,[48] as well as the pure DFT functional TPSS,[49] in conjunction with various basis sets to determine an appropriate theoretical model for the characterisation of **3** (Tables S4–S6, ESI†). The crystallographic distances and angles of **3** were most accurately reproduced with the hybrid TPSSh functional, using a mixed basis set description with the 6-31G(d,p)[52–54] basis set for O, N, C and H atoms, and def2-SV(P)[50,51] basis set for Y atoms, including the intrinsic 28 in-core electron pseudopotential. Thus, the TPSSh/def2-TZVP&6-311G(d,p) method was employed to compute all subsequent calculations and the minimum structures were confirmed by the absence of imaginary frequencies in analytical frequency calculations. The highest occupied molecular orbital of **3** was computed to be predominantly localized on the metallocene and phenolate moieties of the salophen ligand (Fig. 7). The orbital contribution from metallocene moieties features an in-phase combination of yttrium 4d-orbitals with the π-system of the Cp* ligands, while an out-of-phase interaction between the donor atoms of the $(^{tBu}\text{salophen})^{2-}$ ligand and the metal centre could be observed. This lack of orbital symmetry and overlap between the metal centres and diamagnetic bridging ligand, may suggest that the contracted 4f-orbitals of **1** and **2** could also exhibit such ionic bonding interactions, consistent with the weak intramolecular antiferromagnetic coupling observed in **1**. In addition, the lowest unoccupied molecular

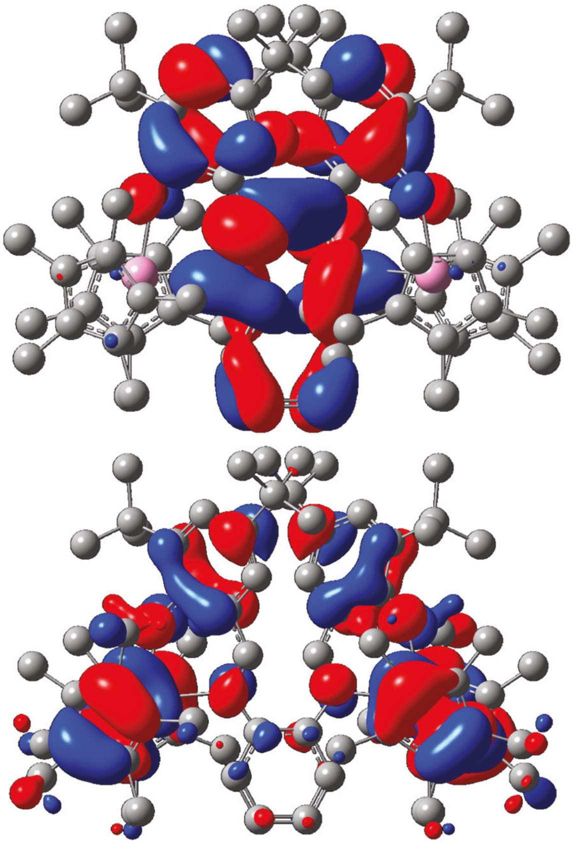

Fig. 7 Frontier molecular orbitals of **3**. Calculated lowest unoccupied molecular orbital (top) and highest occupied molecular orbital (bottom) of $(Cp^*{}_2Y)_2(\mu\text{-}^{tBu}salophen)$, **3**, as computed with TPSSh/def2-TZVP&6-311G(d,p).

orbital of **3** was determined to be almost entirely centred on the bridging salophen ligand, with a negligible contribution from the Cp* ligands (Fig. 7).

Conclusions

The first crystallographically characterised salophen-bridged metallocene complexes, $(Cp^*{}_2RE)_2(\mu\text{-}^{tBu}salophen)$, where RE = Gd (**1**), Dy (**2**), and Y (**3**), for any metal were isolated. The compounds represent simultaneously the first organometallic lanthanide complexes bearing a salophen ligand. The ^1H, ^{13}C, and ^{89}Y NMR signals for **3** were unequivocally assigned, and its diamagnetism allowed for DFT calculations which revealed that the highest occupied molecular orbital is mainly localized on the metallocene and phenolate moieties of the ^{tBu}salophen ligand, indicating the presence of weak coupling between metal centres in **1** and **2** through the ^{tBu}salophen bridge. The magnetic exchange was quantified for **1** and appears to be remarkably weak which is ascribed to the large entity bridging the two lanthanide ions, as supported by the DFT calculations. The present orbital picture is expected to change dramatically upon uptake of an electron, ushering in a diffuse orbital able to penetrate the core electron density of the contracted 4f-orbitals and thus, to boost the magnetic exchange coupling enormously. Notably, cyclic voltammograms for all compounds uncovered quasi-reversible features, which is exciting to the notion that radical-bridged complexes may be indeed realized by chemical means as the redox potentials are readily accessible with commonly used chemical reducing agents. We hypothesize that the quasi-reversable feature may be attributed to the ($^{tBu}salophen^{2-}/^{tBu}salophen^{3-\bullet}$) redox couple, where the 3− oxidation state may correspond to an open shell ligand able to promote magnetic exchange due to its diffuse spin orbital. Increasing the magnitude of J will mitigate quantum tunnelling pathways and result in slower magnetic relaxation oftentimes, yielding magnetic hysteresis with remanence. Compound **2** showed signatures of single-molecule magnet behaviour under a 1000 Oe dc field. The out-of-phase components of the ac magnetic susceptibility were described by considering Raman and Orbach relaxation processes, hinting at the relaxation to occur through virtual excited states and thermally activated regimes, respectively, at the given temperatures. Augmenting the magnetic coupling between the metal centres will drastically alter the temperature window for these relaxation processes to occur, and likely suppress QTM pathways. The highly tuneable salophen ligand allows for multiple substitutions which would directly impact the electronic and magnetic properties and thus, affords a unique platform to investigate magneto-structural correlations in multinuclear organolanthanide single-molecule magnets.

Conflicts of interest

The authors have no financial conflicts to declare.

Acknowledgements

S. D. is grateful to the Department of Chemistry at Michigan State University (MSU) for generous start-up funds. We are grateful to Dr. Daniel Holmes (MSU) for assistance with NMR data and to Prof. James K. McCusker (MSU) for providing access to the UV-Vis-NIR spectrometer. This work was supported in part through computational resources and services provided by the Institute for Cyber-Enabled Research, as well as the Max T. Rodgers NMR facility at MSU. Funding for the single-crystal X-ray diffractometer was provided through the MRI program by the National Science Foundation under Grant No. 1919565.

Notes and references

1 M. Mazzanti, S. Gambarotta, C. Floriani, A. Chiesi-Villa and C. Guastini, Vanadium(III)-Schiff Base Complexes: A Synthetic and Structural Study, *Inorg. Chem.*, 1986, **25**, 2308–2314.

2 N. K. Dutt and K. Nag, Chemistry of lanthanons-XVII. Bis-salicylaldehyde ethylenediamine and bis-salicylaldehyde *o*-phenylenediamine complexes of rare-earths, *J. Inorg. Nucl. Chem.*, 1968, **30**, 2493–2499.

3 T. Radoske, J. März, M. Patzschke, P. Kaden, O. Walter, M. Schmidt and T. Stumpf, Bonding Trends in Tetravalent Th–Pu Monosalen Complexes, *Chem. – Eur. J.*, 2020, **26**, 16853–16859.

4 H. Chen, J. A. Cronin and R. D. Archer, Synthesis and Characterization of Two New Schiff-Bases and Their Soluble Linear Cerium(IV) Polymers, *Inorg. Chem.*, 1995, **34**, 2306–2315.

5 C. Camp, V. Guidal, B. Biswas, J. Pécaut, L. Dubois and M. Mazzanti, Multielectron redox chemistry of lanthanide Schiff-base complexes, *Chem. Sci.*, 2012, **3**, 2433–2448.

6 A. A. Isse, A. Gennaro and E. Vianello, Electrochemical reduction of Schiff base ligands H_2salen and H_2salophen, *Electrochim. Acta*, 1997, **42**, 2065–2071.

7 S. Gambarotta, C. Floriani, A. Chiesi-Villa and C. Guastini, Carbon-carbon bond formation and cleavage resulting from a long-range metal-promoted redox process in the reactions of nickel(II) complexes of *N*,*N*′-*o*-phenylenebis(salicylideneamine), *J. Chem. Soc., Chem. Commun.*, 1982, 756–758.

8 C. Camp, V. Mougel, P. Horeglad, J. Pécaut and M. Mazzanti, Multielectron Redox Reactions Involving C–C Coupling and Cleavage in Uranium Schiff Base Complexes, *J. Am. Chem. Soc.*, 2010, **132**, 17374–17377.

9 E. Gallo, E. Solari, N. Re, C. Floriani, A. Chiesi-Villa and C. Rizzoli, Carbon–Carbon Bonds Functioning as Electron Shuttles: The Generation of Electron-Rich Manganese(II)–Schiff Base Complexes and Their Redox Chemistry, *J. Am. Chem. Soc.*, 1997, **119**, 5144–5154.

10 J. Andrez, V. Guidal, R. Scopelliti, J. Pécaut, S. Gambarelli and M. Mazzanti, Ligand and Metal Based Multielectron Redox Chemistry of Cobalt Supported by Tetradentate Schiff Bases, *J. Am. Chem. Soc.*, 2017, **139**, 8628–8638.

11 N. H. Campbell, N. H. A. Karim, G. N. Parkinson, M. Gunaratnam, V. Petrucci, A. K. Todd, R. Vilar and S. Neidle, Molecular Basis of Structure–Activity Relationships between Salphen Metal Complexes and Human Telomeric DNA Quadruplexes, *J. Med. Chem.*, 2012, **55**, 209–222.

12 K. I. Ansari, J. D. Grant, S. Kasiri, G. Woldemariam, B. Shrestha and S. S. Mandal, Manganese(III)-salens induce tumor selective apoptosis in human cells, *J. Inorg. Biochem.*, 2009, **103**, 818–826.

13 E. A. Mikhalyova, A. V. Yakovenko, M. Zeller, K. S. Gavrilenko, S. E. Lofland, A. W. Addison and V. V. Pavlishchuk, Structure, magnetic and luminescence properties of the lanthanide complexes $Ln_2(Salphen)_3 \cdot H_2O$ (Ln = Pr, Nd, Sm, Eu, Gd, Tb, Dy; H_2Salphen = *N*,*N*′-bis(salicylidene)-1,2-phenylenediamine), *Inorg. Chim. Acta*, 2014, **414**, 97–104.

14 R. D. Archer, H. Chen and L. C. Thompson, Synthesis, Characterization, and Luminescence of Europium(III) Schiff Base Complexes, *Inorg. Chem.*, 1998, **37**, 2089–2095.

15 P.-H. Lin, W.-B. Sun, M.-F. Yu, G.-M. Li, P.-F. Yan and M. Murugesu, An unsymmetrical coordination environment leading to two slow relaxation modes in a Dy_2 single-molecule magnet, *Chem. Commun.*, 2011, **47**, 10993.

16 F. Yang, P. Yan, Q. Li, P. Chen and G. Li, Salen-Type Triple-Decker Trinuclear Dy_3 Complexes Showing Slow Magnetic Relaxation Behavior, *Eur. J. Inorg. Chem.*, 2012, **2012**, 4287–4293.

17 P.-H. Lin, W.-B. Sun, Y.-M. Tian, P.-F. Yan, L. Ungur, L. F. Chibotaru and M. Murugesu, Ytterbium can relax slowly too: a field-induced Yb_2 single-molecule magnet, *Dalton Trans.*, 2012, **41**, 12349.

18 H. Chen and R. D. Archer, Synthesis and Characterization of Lanthanide(III) (La, Gd, Yb, Y) Disalicylidene-1,2-phenylenediamine (H_2dsp) Schiff-Base Complexes, *Inorg. Chem.*, 1994, **33**, 5195–5202.

19 M. N. Leuenberger and D. Loss, Quantum computing in molecular magnets, *Nature*, 2001, **410**, 789–793.

20 G. Karotsis, M. Evangelisti, S. J. Dalgarno and E. K. Brechin, A calix[4]arene 3*d*/4*f* magnetic cooler, *Angew. Chem., Int. Ed.*, 2009, **48**, 9928–9931.

21 C. A. P. Goodwin, F. Ortu, D. Reta, N. F. Chilton and D. P. Mills, Molecular magnetic hysteresis at 60 kelvin in dysprosocenium, *Nature*, 2017, **548**, 439–442.

22 F.-S. Guo, B. M. Day, Y.-C. Chen, M.-L. Tong, A. Mansikkamäki and R. A. Layfield, A Dysprosium Metallocene Single-Molecule Magnet Functioning at the Axial Limit, *Angew. Chem., Int. Ed.*, 2017, **56**, 11445–11449.

23 F. Guo, B. M. Day, Y. Chen, M. Tong, A. Mansikkamäki and R. A. Layfield, Corrigendum: A Dysprosium Metallocene Single–Molecule Magnet Functioning at the Axial Limit, *Angew. Chem., Int. Ed.*, 2020, **59**, 18844–18844.

24 F. S. Guo, B. M. Day, Y. C. Chen, M. L. Tong, A. Mansikkamäki and R. A. Layfield, Magnetic hysteresis up to 80 kelvin in a dysprosium metallocene single-molecule magnet, *Science*, 2018, **362**, 1400–1403.

25 S. Demir, M. I. Gonzalez, L. E. Darago, W. J. Evans and J. R. Long, Giant coercivity and high magnetic blocking temperatures for N_2^{3-} radical-bridged dilanthanide complexes upon ligand dissociation, *Nat. Commun.*, 2017, **8**, 2144.

26 C. N. Carlson, C. J. Kuehl, R. E. Da Re, J. M. Veauthier, E. J. Schelter, A. E. Milligan, B. L. Scott, E. D. Bauer, J. D. Thompson, D. E. Morris and K. D. John, Ytterbocene charge-transfer molecular wire complexes, *J. Am. Chem. Soc.*, 2006, **128**, 7230–7241.

27 C. L. Webster, J. E. Bates, M. Fang, J. W. Ziller, F. Furche and W. J. Evans, Density Functional Theory and X-ray Analysis of the Structural Variability in η^5,η^5,η^1-Tris(ring) Rare Earth/Actinide Tetramethylpyrrolyl Complexes, $(C_5Me_5)_2M(NC_4Me_4)$, *Inorg. Chem.*, 2013, **52**, 3565–3572.

28 F. Delano IV, E. Castellanos, J. McCracken and S. Demir, A Rare Earth Metallocene Containing a 2,2′-Azopyridyl Radical Anion, *Chem. Sci.*, 2021, **12**, 15219–15228.

29 C. A. Gould, E. Mu, V. Vieru, L. E. Darago, K. Chakarawet, M. I. Gonzalez, S. Demir and J. R. Long, Substituent Effects

on Exchange Coupling and Magnetic Relaxation in 2,2′-Bipyrimidine Radical-Bridged Dilanthanide Complexes, *J. Am. Chem. Soc.*, 2020, **142**, 21197–21209.

30 S. Demir, J. M. Zadrozny, M. Nippe and J. R. Long, Exchange Coupling and Magnetic Blocking in Bipyrimidyl Radical-Bridged Dilanthanide Complexes, *J. Am. Chem. Soc.*, 2012, **134**, 18546–18549.

31 C. A. Gould, L. E. Darago, M. I. Gonzalez, S. Demir and J. R. Long, A Trinuclear Radical-Bridged Lanthanide Single-Molecule Magnet, *Angew. Chem., Int. Ed.*, 2017, **56**, 10103–10107.

32 S. Demir, K. R. Meihaus and J. R. Long, Slow magnetic relaxation in a neodymium metallocene tetraphenylborate complex, *J. Organomet. Chem.*, 2018, **857**, 164–169.

33 S. Demir, J. M. Zadrozny and J. R. Long, Large Spin-Relaxation Barriers for the Low-Symmetry Organolanthanide Complexes [$Cp^*_2Ln(BPh_4)$] (Cp*=pentamethylcyclopentadienyl; Ln=Tb, Dy), *Chem. – Eur. J.*, 2014, **20**, 9524–9529.

34 W. J. Evans, S. A. Kozimor, J. W. Ziller and N. Kaltsoyannis, Structure, Reactivity, and Density Functional Theory Analysis of the Six-Electron Reductant, [$(C_5Me_5)_2U]_2(\mu$-η^6:η^6-C_6H_6), Synthesized via a New Mode of $(C_5Me_5)_3M$ Reactivity, *J. Am. Chem. Soc.*, 2004, **126**, 14533–14547.

35 B. J. Barker and P. G. Sears, Conductance behavior of some ammonium and partially substituted ammonium tetraphenylborates in 3-methyl-2-oxazolidone and 3-*tert*-butyl-2-oxazolidone at 25°, *J. Phys. Chem.*, 1974, **78**, 2687–2688.

36 S. Stoll and A. Schweiger, EasySpin, a comprehensive software package for spectral simulation and analysis in EPR, *J. Magn. Reson.*, 2006, **178**, 42–55.

37 G. M. Sheldrick, SHELXT – Integrated space-group and crystal-structure determination, *Acta Crystallogr., Sect. A: Found. Adv.*, 2015, **71**, 3–8.

38 G. M. Sheldrick, Crystal structure refinement with SHELXL, *Acta Crystallogr., Sect. C: Struct. Chem.*, 2015, **71**, 3–8.

39 O. V. Dolomanov, L. J. Bourhis, R. J. Gildea, J. A. K. Howard and H. Puschmann, OLEX2 : a complete structure solution, refinement and analysis program, *J. Appl. Crystallogr.*, 2009, **42**, 339–341.

40 E. Kolehmainen, *Encyclopedia of Spectroscopy and Spectrometry*, Elsevier, 2017, pp. 366–374.

41 G. C. Levy, P. L. Rinaldi and J. T. Bailey, Yttrium-89 NMR. A possible spin relaxation probe for studying metal ion interactions with organic ligands, *J. Magn. Reson.*, 1980, **40**, 167–173.

42 J. Kronenbitter and A. Schwenk, A new technique for measuring the relaxation times T_1 and T_2 and the equilibrium magnetization M_0 of slowly relaxing systems with weak NMR signals, *J. Magn. Reson.*, 1977, **25**, 147–165.

43 G. A. Bain and J. F. Berry, Diamagnetic Corrections and Pascal's Constants, *J. Chem. Educ.*, 2008, **85**, 532.

44 O. Kahn, *Molecular Magnetism*, VCH Publishers, Inc., New York, Weinheim, NY, 1st edn, 1993.

45 M. J. Frisch, G. W. Trucks, H. B. Schlegel, G. E. Scuseria, M. A. Robb, J. R. Cheeseman, G. Scalmani, V. Barone, G. A. Petersson, H. Nakatsuji, X. Li, M. Caricato, A. V. Marenich, J. Bloino, B. G. Janesko, R. Gomperts, B. Mennucci, H. P. Hratchian, J. V. Ortiz, A. F. Izmaylov, J. L. Sonnenberg, D. Williams-Young, F. Ding, F. Lipparini, F. Egidi, J. Goings, B. Peng, A. Petrone, T. Henderson, D. Ranasinghe, V. G. Zakrzewski, J. Gao, N. Rega, G. Zheng, W. Liang, M. Hada, M. Ehara, K. Toyota, R. Fukuda, J. Hasegawa, M. Ishida, T. Nakajima, Y. Honda, O. Kitao, H. Nakai, T. Vreven, K. Throssell, J. A. J. Montgomery, J. E. Peralta, F. Ogliaro, M. J. Bearpark, J. J. Heyd, E. N. Brothers, K. N. Kudin, V. N. Staroverov, T. A. Keith, R. Kobayashi, J. Normand, K. Raghavachari, A. P. Rendell, J. C. Burant, S. S. Iyengar, J. Tomasi, M. Cossi, J. M. Millam, M. Klene, C. Adamo, R. Cammi, J. W. Ochterski, R. L. Martin, K. Morokuma, O. Farkas, J. B. Foresman and D. J. Fox, *Gaussian 16, Revision B.01*, Gaussian, Inc., Wallingford, CT, 2016.

46 S. Grimme, J. Antony, S. Ehrlich and H. Krieg, A consistent and accurate ab initio parametrization of density functional dispersion correction (DFT-D) for the 94 elements H-Pu, *J. Chem. Phys.*, 2010, **132**, 154104.

47 A. D. Becke, Density–functional thermochemistry. III. The role of exact exchange, *J. Chem. Phys.*, 1993, **98**, 5648–5652.

48 V. N. Staroverov, G. E. Scuseria, J. Tao and J. P. Perdew, Comparative assessment of a new nonempirical density functional: Molecules and hydrogen-bonded complexes, *J. Chem. Phys.*, 2003, **119**, 12129–12137.

49 J. Tao, J. P. Perdew, V. N. Staroverov and G. E. Scuseria, Climbing the Density Functional Ladder: Nonempirical Meta–Generalized Gradient Approximation Designed for Molecules and Solids, *Phys. Rev. Lett.*, 2003, **91**, 146401–146404.

50 D. Andrae, U. Häußermann, M. Dolg, H. Stoll and H. Preuß, Energy-adjusted ab initio pseudopotentials for the second and third row transition elements, *Theor. Chim. Acta*, 1990, **77**, 123–141.

51 F. Weigend and R. Ahlrichs, Balanced basis sets of split valence, triple zeta valence and quadruple zeta valence quality for H to Rn: Design and assessment of accuracy, *Phys. Chem. Chem. Phys.*, 2005, **7**, 3297.

52 P. C. Hariharan and J. A. Pople, The influence of polarization functions on molecular orbital hydrogenation energies, *Theor. Chim. Acta*, 1973, **28**, 213–222.

53 R. Ditchfield, W. J. Hehre and J. A. Pople, Self–Consistent Molecular–Orbital Methods. IX. An Extended Gaussian–Type Basis for Molecular–Orbital Studies of Organic Molecules, *J. Chem. Phys.*, 1971, **54**, 724–728.

54 W. J. Hehre, R. Ditchfield and J. A. Pople, Self—Consistent Molecular Orbital Methods. XII. Further Extensions of Gaussian—Type Basis Sets for Use in Molecular Orbital Studies of Organic Molecules, *J. Chem. Phys.*, 1972, **56**, 2257–2261.

55 T. Clark, J. Chandrasekhar, G. W. Spitznagel and P. V. R. Schleyer, Efficient diffuse function-augmented basis sets for anion calculations. III. The 3-21+G basis set for first-row elements, Li-F, *J. Comput. Chem.*, 1983, **4**, 294–301.

56 R. Krishnan, J. S. Binkley, R. Seeger and J. A. Pople, Self–consistent molecular orbital methods. XX. A basis set for correlated wave functions, *J. Chem. Phys.*, 1980, **72**, 650–654.

57 C. Janiak, A. C. Chamayou, A. K. M. Royhan Uddin, M. Uddin, K. S. Hagen and M. Enamullah, Polymorphs, enantiomorphs, chirality and helicity in $[Rh(N,O)(\eta^4\text{-cod})]$ complexes with (N,O) = salicylaldiminato Schiff base or aminocarboxylato ligands, *J. Chem. Soc., Dalton Trans.*, 2009, **9226**, 3698–3709.

58 J. Long, A. O. Tolpygin, E. Mamontova, K. A. Lyssenko, D. Liu, M. D. Albaqami, L. F. Chibotaru, Y. Guari, J. Larionova and A. A. Trifonov, An unusual mechanism of building up of a high magnetization blocking barrier in an octahedral alkoxide Dy^{3+}-based single-molecule magnet, *Inorg. Chem. Front.*, 2021, **8**, 1166–1174.

59 S. Demir, M. D. Boshart, J. F. Corbey, D. H. Woen, M. I. Gonzalez, J. W. Ziller, K. R. Meihaus, J. R. Long and W. J. Evans, Slow Magnetic Relaxation in a Dysprosium Ammonia Metallocene Complex, *Inorg. Chem.*, 2017, **56**, 15049–15056.

60 F.-S. Guo and R. A. Layfield, Strong direct exchange coupling and single-molecule magnetism in indigo-bridged lanthanide dimers, *Chem. Commun.*, 2017, **53**, 3130–3133.

61 R. D. Shannon, Revised effective ionic radii and systematic studies of interatomic distances in halides and chalcogenides, *Acta Crystallogr., Sect. A: Cryst. Phys., Diffr., Theor. Gen. Crystallogr.*, 1976, **32**, 751–767.

62 L. Lumata, A. K. Jindal, M. E. Merritt, C. R. Malloy, A. D. Sherry and Z. Kovacs, DNP by Thermal Mixing under Optimized Conditions Yields >60 000-fold Enhancement of ^{89}Y NMR Signal, *J. Am. Chem. Soc.*, 2011, **133**, 8673–8680.

63 W. J. Evans, J. H. Meadows, A. G. Kostka and G. L. Closs, Yttrium-89 NMR spectra of organoyttrium complexes, *Organometallics*, 1985, **4**, 324–326.

64 R. E. White and T. P. Hanusa, Prediction of ^{89}Y NMR Chemical Shifts in Organometallic Complexes with Density Functional Theory, *Organometallics*, 2006, **25**, 5621–5630.

65 C. J. Schaverien, Alkoxides as Ancillary Ligands in Organolanthanide Chemistry: Synthesis of, Reactivity of, and Olefin Polymerization by the μ-Hydride-μ-Alkyl Compounds $[Y(C_5Me_5)(OC_6H_3{}^tBu_2)]_2(\mu\text{-H})(\mu\text{-alkyl})$, *Organometallics*, 1994, **13**, 69–82.

66 N. F. Chilton, R. P. Anderson, L. D. Turner, A. Soncini and K. S. Murray, PHI: A powerful new program for the analysis of anisotropic monomeric and exchange-coupled polynuclear *d*- and *f*-block complexes, *J. Comput. Chem.*, 2013, **34**, 1164–1175.

67 J. Tang, I. Hewitt, N. T. Madhu, G. Chastanet, W. Wernsdorfer, C. E. Anson, C. Benelli, R. Sessoli and A. K. Powell, Dysprosium triangles showing single-molecule magnet behavior of thermally excited spin states, *Angew. Chem., Int. Ed.*, 2006, **45**, 1729–1733.

68 J. Luzon, K. Bernot, I. J. Hewitt, C. E. Anson, A. K. Powell and R. Sessoli, Spin chirality in a molecular dysprosium triangle: The archetype of the noncollinear ising model, *Phys. Rev. Lett.*, 2008, **100**, 1–4.

69 Y. Gao, G. F. Xu, L. Zhao, J. Tang and Z. Liu, Observation of slow magnetic relaxation in discrete dysprosium cubane, *Inorg. Chem.*, 2009, **48**, 11495–11497.

70 Y. Z. Zheng, Y. Lan, C. E. Anson and A. K. Powell, Anion-perturbed magnetic slow relaxation in planar $\{Dy_4\}$ clusters, *Inorg. Chem.*, 2008, **47**, 10813–10815.

71 H. L. C. Feltham, R. Cle, L. Ungur, V. Vieru, L. F. Chibotaru, A. K. Powell and S. Brooker, Synthesis and Magnetic Properties of a New Family of Macrocyclic, *Inorg. Chem.*, 2012, 10603–10612.

72 T. C. Stamatatos, S. J. Teat, W. Wernsdorfer and G. Christou, Enhancing the quantum properties of manganese-lanthanide single-molecule magnets: Observation of quantum tunneling steps in the hysteresis loops of a $\{Mn_{12}Gd\}$ cluster, *Angew. Chem., Int. Ed.*, 2009, **48**, 521–524.

73 R. A. Layfield, J. J. W. McDouall, S. A. Sulway, F. Tuna, D. Collison and R. E. P. Winpenny, Influence of the *N*-bridging ligand on magnetic relaxation in an organometallic dysprosium single-molecule magnet, *Chem. – Eur. J.*, 2010, **16**, 4442–4446.

74 B. M. Day, F.-S. Guo and R. A. Layfield, Cyclopentadienyl Ligands in Lanthanide Single-Molecule Magnets: One Ring To Rule Them All?, *Acc. Chem. Res.*, 2018, **51**, 1880–1889.

75 Y. Meng, J. Xiong, M. Yang, Y. Qiao, Z. Zhong, H. Sun, J. Han, T. Liu, B. Wang and S. Gao, Experimental Determination of Magnetic Anisotropy in Exchange–Bias Dysprosium Metallocene Single–Molecule Magnets, *Angew. Chem., Int. Ed.*, 2020, **59**, 13037–13043.

76 P. Evans, D. Reta, C. A. P. Goodwin, F. Ortu, N. F. Chilton and D. P. Mills, A double-dysprosocenium single-molecule magnet bound together with neutral ligands, *Chem. Commun.*, 2020, **56**, 5677–5680.

77 H. L. C. Feltham and S. Brooker, Review of purely 4*f* and mixed-metal n*d*-4f, single-molecule magnets containing only one lanthanide ion, *Coord. Chem. Rev.*, 2014, **276**, 1–33.

78 D. Reta and N. F. Chilton, Uncertainty estimates for magnetic relaxation times and magnetic relaxation parameters, *Phys. Chem. Chem. Phys.*, 2019, **21**, 23567–23575.

79 C. E. Jackson, I. P. Moseley and J. M. Zadrozny, A reaction-coordinate perspective of magnetic relaxation, *Chem. Soc. Rev.*, 2021, **50**, 6684–6699.

80 D. Aravena and E. Ruiz, Spin dynamics in single-molecule magnets and molecular qubits, *Dalton Trans.*, 2020, **49**, 9916–9928.

81 S. Demir, I. R. Jeon, J. R. Long and T. D. Harris, Radical ligand-containing single-molecule magnets, *Coord. Chem. Rev.*, 2015, **289–290**, 149–176.